5. INITIAL PAYLOAD CALIBRATION

This chapter summarises the initial activities performed at ESOC to calibrate and monitor the health of the payload prior to the start of routine operations. These calibration activities corresponded to mission critical performance aspects related to the detectors (noise, detector 'piloting', and single-slit responses of the star mapper), and to the optical distortion, focusing, chromaticity, and straylight.

5.1. Calibration Plan

Before the start of routine operations, a series of geometric and photometric calibrations were undertaken in orbit, in order to verify the payload performances in mission critical areas, and to determine the system response and geometrical transformation parameters necessary for the conduct of the mission itself. For the geostationary mission, about 20 days would have sufficed to calibrate both nominal and redundant detection chains. The revised orbit (with a period of 10.66 hours) caused this time to increase significantly due to the greatly reduced observation time, the satellite only being able to collect calibration data when: (a) there was ground station coverage, (b) there were no occultations by Earth or Moon, (c) on-board real-time attitude determination was converged, and (d) the satellite was outside regions of high background noise (the van Allen radiation belts).

The following geometric calibrations were performed by ESOC, according to the chronological order shown in Figure 5.1: (a) transformation of a star's grid coordinates into image dissector tube piloting currents (including non-linearity of the image dissector tube, rigid body displacement of the image dissector tube with respect to the grid, transverse offset of the transformation, and longitudinal offset of the transformation); and (b) chromaticity of the main field of view. In addition, the following photometric calibrations were performed: (c) detector noise, (d) modulation factors for the image dissector tube signal, (e) detector background and straylight counting rates, (f) sensitivity of the instantaneous field of view of the image dissector tube, and (g) single-slit response of the star mapper grids.

Many results from the calibration activities had a direct feedback into satellite operations. For example, the calibration of the star mapper single slit response was used to optimise

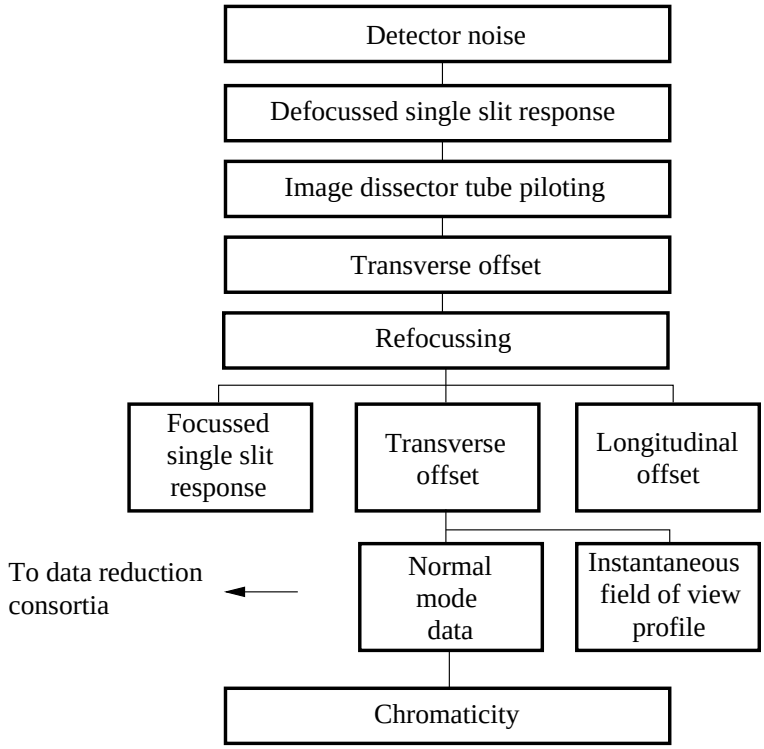

Figure 5.1. *Calibration operational plan.*

the on-board real-time attitude determination by improving the filter used to process star transits on-board. The results of the calibration of the grid to image dissector tube current transformation were regularly uplinked to the satellite to ensure optimum image dissector tube piloting.

5.2. Detector Noise

There were three detectors operating at any given time: the main grid image dissector tube, the star mapper B_T photomultiplier tube and the star mapper V_T photomultiplier tube. Each detector had a backup in case of failure making a total of six detectors on-board the satellite.

The purpose of the detector noise calibration was to measure the dark count rate of the three detectors as a function of several key parameters such as altitude, and to monitor the daily variation in the count rates. For the nominal mission this would have been rather straightforward. In the revised mission, the orbit with perigee height of about 500 km took the satellite through the Earth radiation (van Allen) belts. In addition, the calibration was performed at a solar maximum and several solar flares were observed e.g. 30 September and 20 October 1989.

Finally, various spacecraft configurations were used, in particular employing detection chains 1 and 2, shutters open and closed, and telescope baffle covers in place and released. Table 5.1 shows the results of several days processing for high altitudes (above 35 000 km). The effect of opening the shutters on 22 September was very small and

Table 5.1. High altitude count rates (above 35 000 km).

Date	Image dissector	Star mapper	Image dissector counts/sec	B_T channel counts/sec	V_T channel counts/sec	Baffle covers	Shutter status
89-09-18	1	1	1.5	8.3×10^2	7.1×10^2	In Place	Closed
89-09-19	1	1	1.9	5.2×10^2	4.8×10^2	In Place	Closed
89-09-22	1	1	3.2	8.3×10^2	7.2×10^2	In Place	Open
89-09-25	2	2	0.8	4.8×10^2	6.1×10^2	In Place	Open
89-09-30	2	2	25.0	5.7×10^4	8.4×10^4	Released	Closed

Table 5.2. Lower altitude count rates (below 35 000 km).

Date	Image dissector	Star mapper	Image dissector counts/sec	B_T channel counts/sec	V_T channel counts/sec	Altitude km	Time from perigee (hours)
89-09-21	1	1	6.6	2.4×10^3	2.0×10^3	30000	3.00
89-09-21	1	1	9.3	4.1×10^3	3.3×10^3	25000	2.21
89-09-21	1	1	22.4	1.1×10^4	8.4×10^3	20000	1.62
89-09-21	1	1	74.2	3.9×10^4	3.1×10^4	15000	1.16
89-09-21	1	1	70.6	3.6×10^4	2.8×10^4	12500	0.95
89-09-21	1	1	28.8	1.1×10^4	8.8×10^3	10000	0.77
89-09-21	1	1	11.8	5.8×10^3	4.6×10^3	8000	0.62
89-09-28	2	2	17.1	4.0×10^4	4.1×10^4	6000	0.49
89-09-28	2	2	169.5	6.1×10^5	4.1×10^5	5000	0.43
89-09-28	2	2	423.7	1.0×10^6	9.5×10^5	4000	0.36
89-09-28	2	2	613.1	1.3×10^6	1.3×10^6	3000	0.28

it was evident that chain 2 performed better than chain 1. The data obtained on 30 September showed the increase in the dark count rate when encountering a solar flare. Under these conditions, it was not easy to obtain good star mapper transits and the on-board real-time attitude determination found it difficult to maintain precise attitude estimates.

Table 5.2 gives the count levels at lower altitudes as a function of altitude for two different orbits (the satellite was not visible for the very low altitudes on 21 September). The passage through the upper radiation belt is clearly seen, with peak count rates obtained on all three detectors at about 15 000 km followed by the rates lowering to a minimum at about 8000 km before rising very rapidly in the lower belt. The values peaked at about 3000 km in the lower radiation belt but it was difficult to get coverage below that altitude due to a lack of ground stations close to the equator. The count rates fell again just below 3000 km before loss of telemetry from the satellite.

The high count rates in the photomultiplier tubes during passage through the van Allen belts, presented difficulties for real-time attitude determination (see Chapter 14). In the lower belt, noise levels were so high that they prevented any stars being detected in the star mapper data stream. This ‘blinding’ at a time when disturbance torques acting on the spacecraft were greatest rendered the real-time attitude determination periodically unable to function on-board after perigee, the real attitude being too far from that

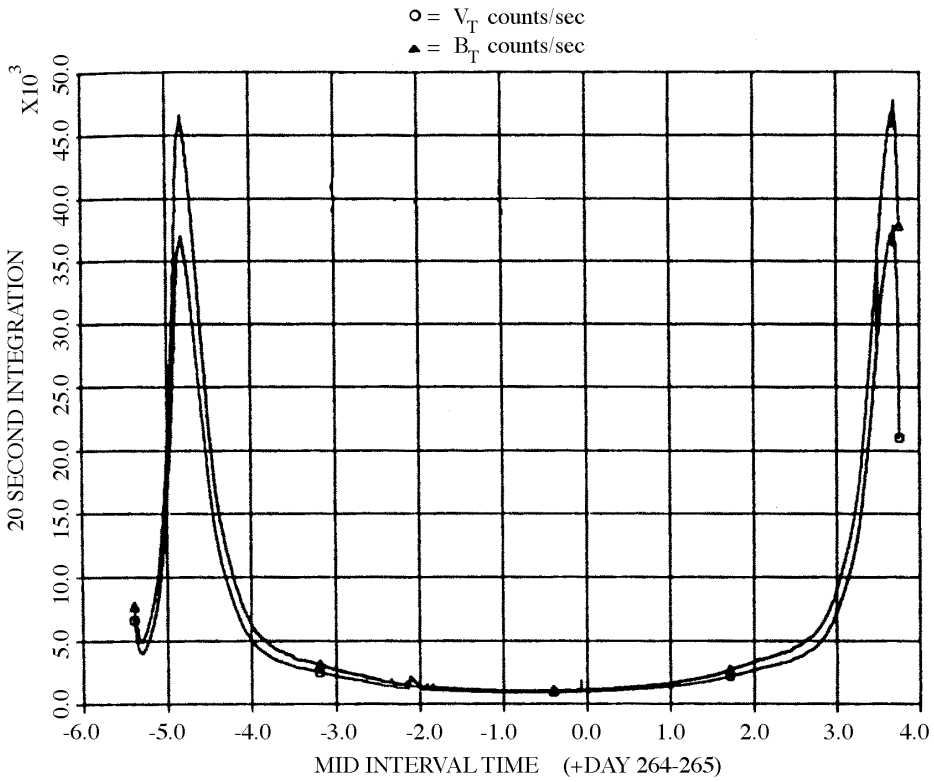

Figure 5.2. *Photomultiplier count rates for one orbit. The central region corresponds to low background count rates at apogee, with the peaks at each side of the figure corresponding to the high background count rates observed during the passage of the satellite through the outer van Allen radiation belts encountered close to perigee.*

estimated on-board. Under these conditions, manual intervention was required from ground to recompute the spacecraft attitude and correct the values held on-board. In the upper belt, it was usually possible to detect the brighter stars above the noise, allowing real-time attitude determination to operate normally. The peak noise and duration of the upper belt was highly dependent on solar activity.

Figure 5.2 shows the background rates obtained for the visibility period of a complete orbit. The two passages through the upper radiation belt are clearly visible.

5.3. Star Mapper Single-Slit Response

The on-board (and on-ground) real-time attitude determination system required accurate star mapper transit measurements. To compute reliable and unambiguous transit times, i.e. accurate times and a good certainty that the correct star had been processed, an accurate representation of the star mapper single-slit response, $S(x)$ defined in Equation 1.2, was necessary. The results of the calibration of this response were used to construct a filter that could be cross-correlated with the raw star mapper data by the on-board computer. The output of the filter allowed the transit time (position of peak) and star magnitude (height of peak) to be computed. The same filter was used by on-ground software during attitude initialisation (see Chapter 14).

The response itself was calibrated by analysing the transits of bright stars, $B < 6$ mag, across the star mapper slits. It was simple, using a filter based on *a priori* knowledge of the slit response and optimised for the actual scanning velocity of the satellite, to compute very accurate transit times for these stars. These transit times, together with pre-launch knowledge of the slit geometry, allowed the relative position of each sample with respect to the slit centres to be determined. All collected data were normalised and a least-squares estimator was used to fit a 12th order polynomial to the collected data subdivided according to B_T or V_T channel, and vertical or inclined slit system. Figure 5.3 shows four typical calibrated responses.

5.4. Initial Image Dissector Tube Piloting

The piloting of the instantaneous field of view of the image dissector tube to a star's image was performed by the on-board computer every $\frac{1}{150}$ s. To do this accurately, the following information was needed by the on-board computer: (i) *a priori* estimate of the star's position, (ii) knowledge of the satellite pointing direction, (iii) knowledge of geometric distortions in the optical system, and (iv) knowledge of the transformation between grid position and image dissector tube piloting currents.

Star Positions

The star positions were uplinked to the on-board computer in the form of a programme star file based on the pre-defined Hipparcos Input Catalogue of stars to be observed. This catalogue contained positional information for about 120 000 pre-selected stars down to a limiting magnitude of $B = 13$ mag. The programme star file produced from the Hipparcos Input Catalogue was defined relative to a nominal scanning law, i.e. the pointing directions of the two fields of view were pre-defined and uniquely identified the stars' expected transit times at the centre of the field of view together with the ordinate and drift angle at the time of transit. All this information was uplinked to the satellite for all stars to be observed. From this information, the stars' positions on the grid as a function of time from the expected transit time could be computed by the on-board computer:

$$\begin{aligned} \eta_N &= \omega_N (t - t_s) \\ \zeta_N &= \zeta_s + \mu_s \omega_N (t - t_s) \end{aligned} \qquad [5.1]$$

where:

(η_N, ζ_N) is the nominal position of the star on the grid (radians)

ω_N is the nominal scanning velocity (radians s^{-1})

t is time (s)

t_s is the expected transit time (s)

ζ_s is the expected ordinate at transit (radians)

μ_s is the drift angle of the star (radians)

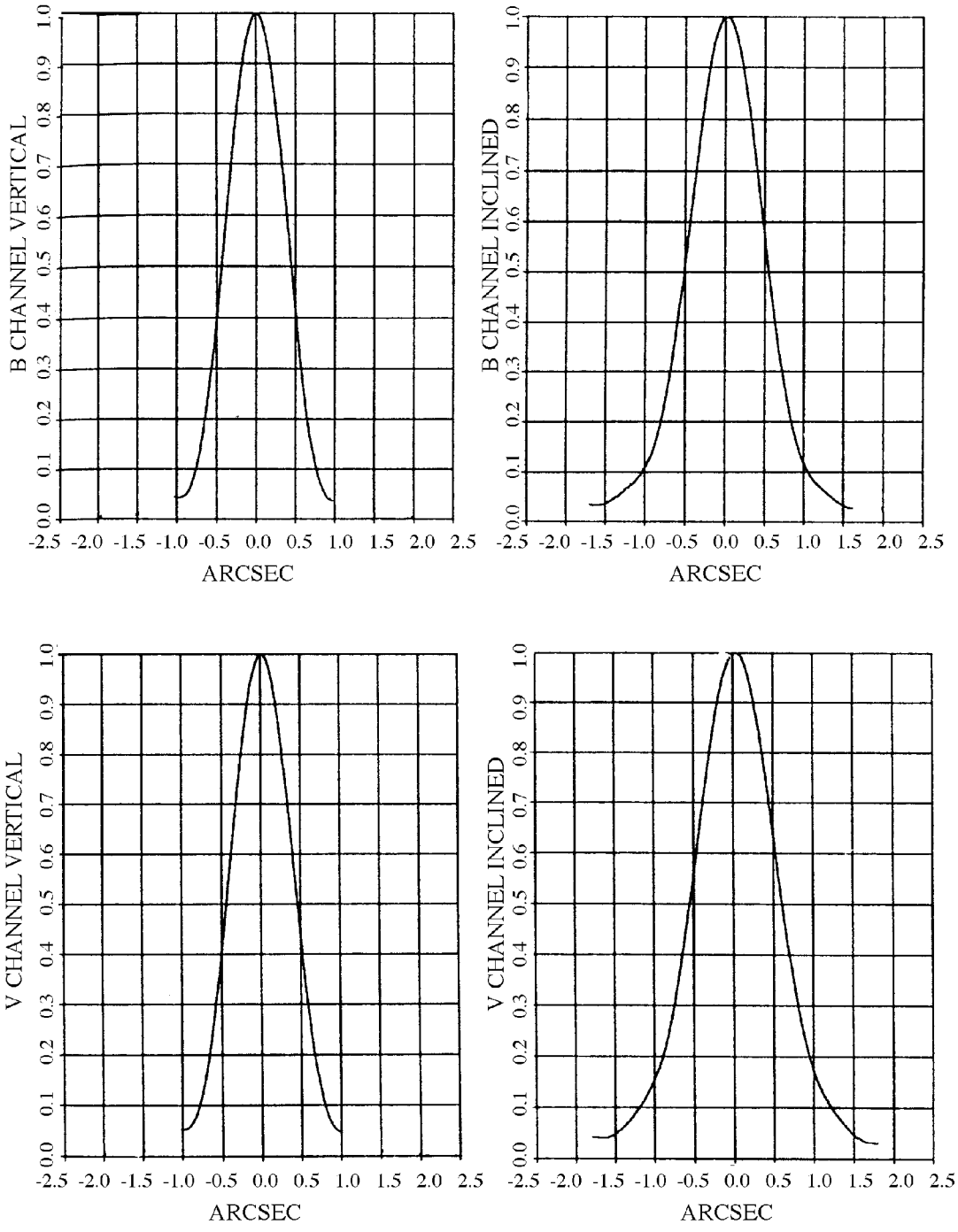

Figure 5.3. *Star mapper single-slit response for the B_T channel (upper pair), the V_T channel (lower pair), and for the vertical (left pair) and inclined (right pair) slits.*

Attitude De-Pointing and Optical Distortion

Equation 5.1 defines the position of the star on the grid assuming a perfect optical system, and assuming that the satellite did not deviate from the nominal scanning law. However, the satellite did not follow this law perfectly but was allowed to drift by up to 10 arcmin along any axis from the nominal. Also, during the initial payload calibration phase, there were the major effects of basic angle error and grid rotation to be compensated for. A final correction was made for the transverse offset of the image dissector tube.

The deviation from the nominal scanning law was computed on-board by the real-time attitude determination software as a set of three Tait-Bryan error angles (ϕ, θ, ψ) and their rates of change with time $(\dot{\phi}, \dot{\theta}, \dot{\psi})$. This is discussed in more detail in Chapter 14.

Applying all these effects together, the equations for the star's grid position (η_C, ζ_C) could be expressed as:

$$\eta_C = \eta_N + (\psi_i + f\frac{\delta\gamma}{2}) + (\mu_i + \mu_{Gi})\zeta_N - \mu_{Gi}\nu_i \qquad [5.2]$$
$$\zeta_C = \zeta_N - \nu_i - (\mu_i + \mu_{Gi})\eta_N - \mu_{Gi}(\psi_i + f\frac{\delta\gamma}{2}) + \delta\zeta_i$$

where:

$\delta\gamma$ is the correction for the basic angle error (radians)

μ_{Gi} is the grid rotation for field of view i (radians)

i is the field of view selector (1=preceding, 2=following)

f is +1 when $i = 1$, and −1 when $i = 2$

$\delta\zeta_i$ is the transverse offset for field of view i (radians)

and:

$$\mu_i = \cos(\frac{\gamma_N}{2})\phi + f\sin(\frac{\gamma_N}{2})\theta$$
$$\nu_i = \cos(\frac{\gamma_N}{2})\theta - f\sin(\frac{\gamma_N}{2})\phi \qquad [5.3]$$
$$\psi_i = \psi + \frac{1}{2}(\phi\theta - \mu_i\nu_i)$$

with γ_N the satellite's nominal basic angle (radians).

Grid Coordinates to Image Dissector Tube Piloting Currents

The electrical piloting of the instantaneous field of view to the computed position of the star's image was performed by the on-board computer using a 'coil current calibration matrix' of 11×11 points defining a regularly spaced mesh on the grid. For each point in the mesh, the electrical currents to pilot to that position were known. Thus, for any given position on the grid, the on-board computer performed a two-dimensional linear interpolation using the four surrounding points of the calibration matrix mesh to compute the best currents for the given position. The computation of the calibration matrix itself was performed by on-ground software in three steps: (i)

using an internal star pattern assembly; (ii) using grid reference marks close to the main grid; (iii) computing the coil current calibration matrix.

Internal Star Pattern Assembly

The calibration of the non-linearity of the image dissector tube piloting was performed using an internal star pattern assembly. This consisted of a pattern of 196 dummy light sources illuminated by two light-emitting diodes (see Section 2.6). These were imaged directly onto the photocathode of the image dissector tube by a switching mirror in the optical path. The on-board computer performed a special cross scan around each of these dummy light sources and on-ground software then analysed the raw telemetry generated and worked out the optimum currents that piloted the sensitive area of the image dissector tube to each of these dummy stars. The result of this calibration was a non-linearity matrix for the image dissector tube but still without any well-defined reference on the grid. This was provided by the next step.

Grid Reference Marks

The rigid body displacement of the image dissector tube with respect to the grid was computed using two fixed grid reference marks. These marks were built into the grid at known positions and illuminated by light-emitting diodes. In a similar way to the internal star pattern assembly calibration, the on-board computer scanned cross patterns around each of the reference marks and on-ground software then computed the best currents to pilot the sensitive area of the image dissector tube to each mark.

Coil Current Calibration Matrix Computation

The best currents computed in the grid reference mark calibration were used to define a transformation matrix that converted between the photocathode and the grid reference frames, i.e. the rotation and translation of the image dissector tube with respect to the grid were then known. The final step in the coil current calibration matrix computation was to use the non-linearity data obtained from the internal star pattern assembly calibration to compute the currents needed to scan to the fixed positions in the coil current calibration matrix mesh. This was achieved by performing a least-squares fit for the best currents using the four closest positions in the non-linearity matrix. If the results were in fairly good agreement with the previous coil current calibration matrix, then the new one was automatically uplinked from the on-ground software to the satellite without manual intervention. The complete cycle of telecommanding, ground processing and uplink of results could be performed automatically, driven by the mission planning software.

5.5. Transverse and Longitudinal Offsets

The first in-orbit calibration of the image dissector tube piloting was performed on 5 October 1989 and it was repeated on 19 October. As well as calibrating the non-linearity of the image dissector tube, through use of the coil current calibration matrix, it was also necessary to assess the constant offset in the transformation of a star's grid coordinates into image dissector tube piloting currents. Two offsets were assessed: in the transverse and longitudinal directions.

Transverse Offset

One effect, compensated for in Equation 5.2, was the addition of the transverse offset, $\delta\zeta_i$ for field of view i. This was caused by the photocentre of the star's image being offset from the telescope's chief ray due to the semi-circular geometry of the field of view entrance pupil. It was calibrated, in-orbit, by dedicated observations made with a modified programme star file. Instead of piloting the image dissector tube to the computed position of the star, the on-board computer piloted the image dissector tube to positions offset from the actual star image. This was achieved by the insertion of 'dummy' stars into the programme star file, with the same transit times as the actual star but with different ordinate values, ζ_s. A pattern of 10 of these 'dummy' stars was placed around each of the actual stars scheduled for observation (generally these were bright stars). By analysing the count rates at each of the 10 positions, the on-ground software could compute the offset from the actual star to the position that gave the highest count rate. By averaging many such observations, the mean offset for each field of view could be computed. The resulting offsets were then uplinked to the satellite.

Longitudinal Offset

The longitudinal offset of the image dissector tube piloting is not directly compensated for in Equation 5.2 as it was expected to be very small. This was verified, in-orbit, by dedicated observations with another modified programme star file. The special programme star file contained 'dummy' stars positioned close to an actual star with the same ordinate, ζ_s, but with modified transit times. Ground software, based on the transverse offset program, was used to compute the mean offset for each field of view. If the absolute value of the result had been the same for each field of view but with opposite sign, it would probably have been due to an error in the basic angle and could have been compensated for by modifying the value of $\delta\gamma$ used in Equation 5.2.

Image Dissector Tube Piloting Offset Results

The offset calibrations were performed four times during the calibration phase. The first calibration was carried out on 13 October 1989 before the telescope refocusing operations had been performed. Only the transverse offsets for each field of view were calibrated. The results obtained were -4.029 and -4.126 arcsec for the preceding and following fields of view respectively.

The transverse offsets were recalibrated on 1 November after refocusing, giving −3.766 and −4.251 arcsec for the preceding and following fields of view respectively. The longitudinal offsets were calibrated for the first time on 3 November after refocusing giving −1.004 and −0.380 arcsec for the preceding and following fields of view respectively.

An analysis was subsequently performed to investigate residual piloting offsets after the previous calibration. As a result, an empirical correction was introduced into the coil current calibration matrix computation. To verify this correction, both longitudinal and transverse offsets were recalibrated on 24 and 25 November 1989. The results for the transverse offsets were in good agreement with those previously obtained. Moreover the revised values for the longitudinal offsets showed a reduced spread of values about the mean, indicating that the empirical correction had been successful.

The grid rotation angle and basic angle (separating the two fields of view) were subsequently calibrated to high accuracy by the data reduction consortia. Corrected values were first used on-board on 23 January 1990, without empirical correction. The transverse offsets were recalibrated, giving −3.797 and −4.219 arcsec for the preceding and following fields of view respectively. These were the values used on-board throughout the rest of the mission. The longitudinal offsets were recalibrated giving −0.306 and −0.300 arcsec for the preceding and following fields of view respectively. The spread in the values obtained for the longitudinal offset showed a further reduction indicating a further improvement. It was not deemed necessary to re-compute any empirical corrections.

5.6. Focusing

The telescope could be refocused using a mechanism that allowed the grid assembly to move with respect to the telescope focal surface (see Section 3.2). This was necessary for two main reasons: (a) to enable the position of best focus to be determined at the start of the mission; and (b) to compensate for effects such as moisture release which altered the focus throughout the mission.

The quality of the focus for any given position of the grid assembly was assessed by ground processing of image dissector tube data collected for bright stars ($B < 9$ mag) in the central portion of a 3×3 subdivision of the main grid. As the focus was improved, the value of the first modulation coefficient, M_1 in Equation 1.1, increased. This value was determined by the ground processing software from 45 minutes of observations for each focus setting, as a function of star colour and field of view. Operationally, data was collected for ten different focus settings close to the predicted beginning-of-life position between 12 and 28 October 1989. The results are presented graphically in Figure 5.4 as a function of three colour groups.

The standard deviations of the residuals from a least-squares parabolic fit varied between 0.9 per cent and 1.9 per cent for the six cases considered.

There was evidence from this for a differential defocus, i.e. the position of best focus was not the same for each field of view. The position of best focus for the preceding field of view after launch was −44 μm and that for the following field of view was −26 μm. The actual position chosen as best overall focus immediately after launch, −35 μm, gave a differential defocus of ±9 μm. In December 1989, a revised grid scale factor was

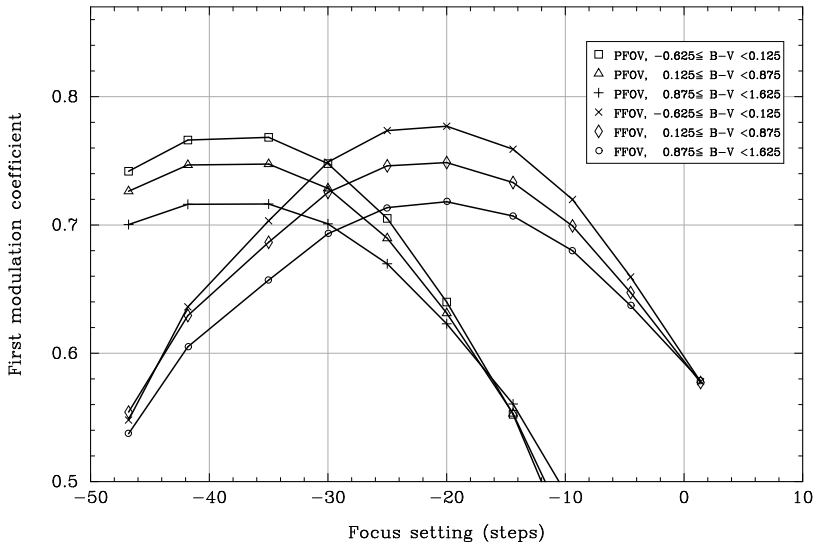

Figure 5.4. *The behaviour of the first modulation coefficient, M_1, versus focus position, and as a function of star colour and field of view. In the legend, PFOV and FFOV refer to results for the preceding and following fields of view respectively. Results are shown for three colour intervals in each case.*

computed by the data reduction consortia which improved the accuracy of observations. This had the effect of increasing the estimates of M_1 by approximately 5 per cent. The results from the calibration were in excellent agreement with pre-launch prediction of the optical performance. As stated above, the position of best focus evolved continuously due to moisture release and other effects (see Chapter 10). The refocusing calibration was performed at regular intervals throughout the mission with the objective of keeping the focus position on-board within one step ($\pm 1.2\ \mu$m) of the best focus position.

5.7. Instantaneous Field Of View Profile

The sensitivity profile of the image dissector tube was defined by a normalised transmission factor, $T(x)$, which defined the proportion of the observed star intensity obtained as the image dissector tube was depointed away from a star by x arcsec. It was important for the data analysis consortia to know this sensitivity profile, in particular for the processing of data for close double stars. The profile was calibrated, in-orbit, using a special programme star file containing 'dummy' stars deliberately positioned away from chosen bright stars. Ground software was used to compute the profile as a function of position in the field of view (on a 3×3 subdivision of the grid), star colour (3 colour groups), and offset distance (in arcsec).

Because of the instantaneous field of view profile's dependency on many parameters, over 20 hours of data between 9 and 21 October 1989 were collected and processed. The average of all profiles computed is shown in Figure 5.5.

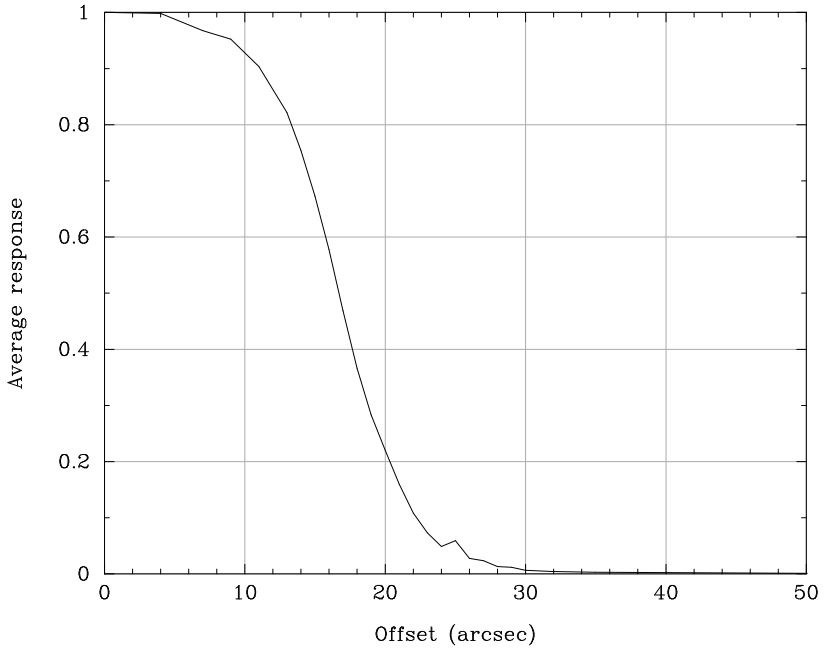

Figure 5.5. *Mean instantaneous field of view profile. The response profile is rather flat within ±10 arcsec from the centre, thereafter dropping steeply towards zero at around ±30 arcsec.*

5.8. Chromaticity

The chromaticity of the main field of view was defined to be the displacement of the photocentre of the image of a star of 'extreme' colour, $B - V = -0.25$ mag or $B - V = 1.25$ mag, compared with the photocentre of a star of typical colour, $B - V = 0.5$ mag. The (very small) chromatic displacement of the star images as a function of colour resulted from the form of the diffraction image, and was calibrated in-orbit using a special filter built into the payload (see Chapter 2). During calibration the filter was moved into the beam, by telecommand, between the grid and the image dissector tube. It caused the image of a star to be split into two images, red and blue, separated by approximately 60 arcsec. By piloting the image dissector tube to the two spots, quasi-simultaneously, data could be collected for further ground processing. This processing consisted of estimating the phase difference between the two image dissector tube signals using Equation 1.1 for each image separately. A resulting chromaticity map was built up, as a function of star colour and position in the field of view.

The associated image dissector tube signals for the two spots were measured, from which a phase difference for the two signals could be calculated. The phase differences were converted to chromaticity estimates by the following formula:

$$C_i = (\Psi_{1,i} - \Psi_{2,i}) \frac{\Delta\lambda}{\Delta\lambda_s} \qquad [5.4]$$

where $\Psi_{1,i}$ is the phase estimate for the blue spot associated with star i, $\Psi_{2,i}$ is the phase estimate for the red spot associated with star i, $\Delta\lambda$ is the effective wavelength difference

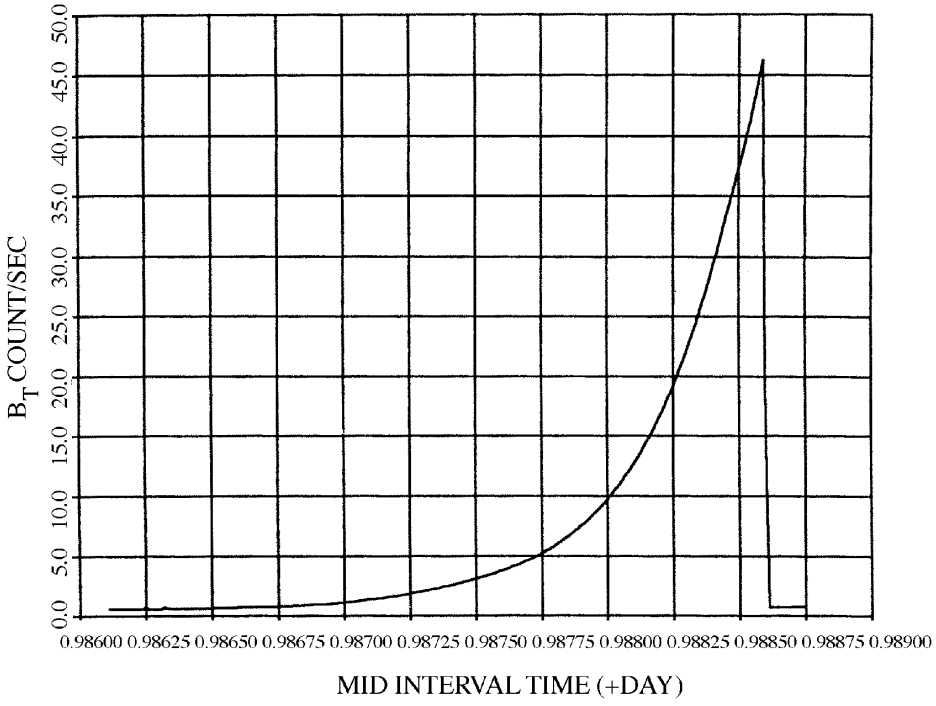

Figure 5.6. *Star mapper background (B_T) leading up to automatic shutter closure on 6 November 1989.*

between the images of a star of extreme colour and one of average colour, and $\Delta\lambda_s$ is the effective wavelength difference of the blue and red star images formed by the chromaticity filter assembly.

Each estimate was allocated a weight computed from the expected variance of the estimation. The final chromaticity map was produced by computing the weighted average of the individual chromaticity estimates in each of the mesh bins.

The first calibration was performed between 22 and 24 November 1989, giving an average value over both fields of view of −0.27 milliarcsec. Subsequently, more refined calibrations were performed by the data reduction consortia (see Volume 3), and the instrumental chromaticity was also estimated from the great-circle and sphere solutions.

5.9. Straylight

Straylight count rates for both star mapper and image dissector tube were calibrated. For the star mapper, background count rates entering and leaving an occultation were measured. Under normal operations, both image dissector tube and star mapper shutters were closed by ground command, for the protection of the detectors themselves. In addition, there was an automatic shutter closure facility on-board the satellite that closed the shutters if the count rate in the B_T channel became too high. This mechanism was exercised on 6 November 1989. The resulting rise in background rates culminating in shutter closure is shown in Figure 5.6.

The telemetry collected during the instantaneous field of view profile calibration also contained many observations away from programme stars permitting measurement of the sky background count rate on the image dissector tube. The algorithm used was to position a dummy star in the programme star file away from the programme stars. Analysis of the image dissector tube data was then performed and the modulation coefficients were computed. Any observation with $M_1 < 0.325$ was rejected and observations close together in time were averaged. In total, there were 3043 observations during this phase of the initial payload calibration, with a mean of 36 counts/sec and standard deviation of 16 counts/sec.